Atmos. Meas. Tech., 8, 907–920, 2015
www.atmos-meas-tech.net/8/907/2015/
doi:10.5194/amt-8-907-2015
© Author(s) 2015. CC Attribution 3.0 License.

Atmospheric Measurement Techniques
Open Access

Quantifying error of lidar and sodar Doppler beam swinging measurements of wind turbine wakes using computational fluid dynamics

J. K. Lundquist[1,2], M. J. Churchfield[2], S. Lee[2], and A. Clifton[2]

[1]Department of Atmospheric and Oceanic Sciences, University of Colorado Boulder, Boulder, Colorado, USA
[2]National Renewable Energy Laboratory, Golden, Colorado, USA

Correspondence to: J. K. Lundquist (julie.lundquist@colorado.edu)

Received: 30 June 2014 – Published in Atmos. Meas. Tech. Discuss.: 12 September 2014
Revised: 12 January 2015 – Accepted: 23 January 2015 – Published: 23 February 2015

Abstract. Wind-profiling lidars are now regularly used in boundary-layer meteorology and in applications such as wind energy and air quality. Lidar wind profilers exploit the Doppler shift of laser light backscattered from particulates carried by the wind to measure a line-of-sight (LOS) velocity. The Doppler beam swinging (DBS) technique, used by many commercial systems, considers measurements of this LOS velocity in multiple radial directions in order to estimate horizontal and vertical winds. The method relies on the assumption of homogeneous flow across the region sampled by the beams. Using such a system in inhomogeneous flow, such as wind turbine wakes or complex terrain, will result in errors.

To quantify the errors expected from such violation of the assumption of horizontal homogeneity, we simulate inhomogeneous flow in the atmospheric boundary layer, notably stably stratified flow past a wind turbine, with a mean wind speed of $6.5\,\mathrm{m\,s^{-1}}$ at the turbine hub-height of 80 m. This slightly stable case results in 15° of wind direction change across the turbine rotor disk. The resulting flow field is sampled in the same fashion that a lidar samples the atmosphere with the DBS approach, including the lidar range weighting function, enabling quantification of the error in the DBS observations. The observations from the instruments located upwind have small errors, which are ameliorated with time averaging. However, the downwind observations, particularly within the first two rotor diameters downwind from the wind turbine, suffer from errors due to the heterogeneity of the wind turbine wake. Errors in the stream-wise component of the flow approach 30 % of the hub-height inflow wind speed close to the rotor disk. Errors in the cross-stream and vertical velocity components are also significant: cross-stream component errors are on the order of 15 % of the hub-height inflow wind speed ($1.0\,\mathrm{m\,s^{-1}}$) and errors in the vertical velocity measurement exceed the actual vertical velocity. By three rotor diameters downwind, DBS-based assessments of wake wind speed deficits based on the stream-wise velocity can be relied on even within the near wake within $1.0\,\mathrm{m\,s^{-1}}$ (or 15 % of the hub-height inflow wind speed), and the cross-stream velocity error is reduced to 8 % while vertical velocity estimates are compromised. Measurements of inhomogeneous flow such as wind turbine wakes are susceptible to these errors, and interpretations of field observations should account for this uncertainty.

1 Introduction

Since the emergence of a modern generation of lidar wind profilers in the mid-2000s, several commercial products have entered the market and have gained wide use for wind energy, air quality, and urban meteorology applications. Procedures have been established for ensuring traceability of the calibration of lidars and documenting uncertainty in lidar measurements (Gottschall et al., 2012; Clifton et al., 2013a). The requirement of plentiful aerosol particles for scattering the signal has been documented (Aitken et al., 2012). Extensive interest in the complex flow in wind farms has inspired the use of both profiling and scanning lidars in wind farms to quantify turbine wakes (Käsler et al., 2010; Ra-

jewski et al., 2013; Rhodes and Lundquist, 2013; Krishnamurthy et al., 2013; Iungo et al., 2013; Smalikho et al., 2013). Dual-Doppler (Newsom et al., 2005, 2015; Stawiarski et al., 2013) and triple-Doppler (Mikkelsen et al., 2008; Mann et al., 2008; Khadiri-Yahzemi et al., 2013) approaches enable the full three-dimensional flow to be resolved. The ability of such instruments to resolve atmospheric turbulence has been explored (Sathe et al., 2011; Sathe and Mann, 2013; Fuertes et al., 2014), and lidar measurements in heterogeneous urban flow have been compared with tower measurements (Lane et al., 2013).

However, when relying on measurements from a single instrument, critical assumptions about the flow are required to estimate three components of the flow (Courtney et al., 2008). Doppler lidars sample the flow over a volume extending along the laser beam. Many lidar wind profilers exploit the Doppler shift of laser light backscattered by particulates carried by the wind. A known frequency of light is emitted from the laser, and the backscattered radiation will have a shift in frequency related to how rapidly particulates are moving toward or away from the laser source along the line of the beam or the line of sight (LOS) (Cariou, 2011). To provide profiles of wind speed and wind direction, many commercially available lidar (and sodar) systems use the Doppler beam swinging (DBS) technique. By shifting the beam between a series of four radial wind directions typically at approximately 60° elevation and perpendicular to each other, the Doppler shift (and therefore the LOS velocity) can be calculated. For pulsed lidars, all altitudes are measured based on the same pulse. Measurements at different heights are identified based on the arrival time of the backscatter compared to the initiation of the pulse.

Typically, the assumption of horizontal homogeneity over a horizontal area is invoked to interpret DBS measurements to calculate horizontal and vertical wind speeds rather than LOS velocities. However, if that assumption of horizontal homogeneity is applied to velocity retrievals in the case of inhomogeneous flow, errors in wind speed estimation will emerge. Cheong et al. (2008) have used coherent radar imaging to assess errors in radar measurements due to the DBS method and find that inhomogeneities in the wind field introduce biases in the DBS measurements.

Although DBS methods have been used with sodar (Barthelmie et al., 2003) and lidar (Nygaard, 2011; Rhodes and Lundquist, 2013; Kumer et al., 2013) to characterize wind turbine wakes, the error in DBS measurements of wind turbine wakes has not yet been quantified. Approaches to quantifying this error have been explored for flow in complex terrain, but not in the context of the inhomogeneous flow near a turbine wake. The effect of complex terrain has been explored analytically (Bingöl et al., 2008) with linear flow models such as WAsP (Bingöl et al., 2009), and with Reynolds-averaged Navier–Stokes (RANS) computational fluid dynamics (CFD) models (Boquet et al., 2010; Harris et al., 2010; Meissner and Boquet, 2011; Bezault and Boquet, 2011; Gkainias et al., 2011; Butler and Quail, 2012; Bradley et al., 2012). Hasager et al. (2013) use RANS CFD to correct measurements in flow over offshore platforms. Wainright et al. (2014) use large-eddy simulation (LES) to simulate fields retrieved by sodar toward error quantification.

To date, LES CFD has not been used to simulate the wind fields as retrieved by lidar with DBS, although LES CFD can quantify the uncertainty in measurements resulting from very inhomogeneous flow such as turbine wakes within the degree of uncertainty of the model. The goal of this study, therefore, is to quantify DBS error in wind turbine wake flows by employing LES of atmospheric boundary-layer flow. The full three-dimensional time-varying flow (both upwind and downwind of a wind turbine) is calculated with the model. From the full flow field, lidar "observations" are retrieved using the DBS scanning strategy, which involves sampling four beams and calculating the components of the flow from four separate LOS velocities. Wind profiles, or simulated towers at the lidar locations, are also extracted from the simulations. The differences between the DBS retrievals and the wind profiles quantify the DBS error in inhomogeneous flow.

To bound the error introduced by inhomogeneity in the flow, we explore a worst-case scenario of a stable atmospheric boundary layer flowing past a wind turbine. Stable layers can often exhibit considerable change of wind direction with height. Further, wind turbine wakes tend to persist longer in stable conditions with minimal background turbulence that can erode the wake, thereby introducing and maintaining significant heterogeneity in the wake. This heterogeneity is expected to challenge the DBS approach. For a lidar using the typical DBS approach with four beams, each 60° from horizontal, two opposing beams are 92 m apart at an altitude of 80 m. This horizontal distance is on the order of modern wind turbine rotor diameters. This large distance is especially problematic for measuring the cross-stream velocity, which is based on beams that span the wake – one beam may measure flow within the wake, while the opposite may be in the free stream or on the opposite side of the wake. Furthermore, the vertical velocity measurement relies on all four beams, and different beams can measure opposite sign vertical velocity, undermining the measurement. The stream-wise velocity measurement relies on the stream-wise beams, so this measurement may be more accurate because the stream-wise velocity gradients are less extreme. However, the gradients of stream-wise velocity with respect to the stream-wise direction are strongest nearest the rotor.

To quantify the effects of these numerous sources of DBS measurement error, we perform LES of stably stratified flow past a wind turbine. We then introduce a series of hypothetical DBS lidar observations, including the lidar weighting function, into the upstream and the waked flow to compare the observations that would have been retrieved by a lidar using DBS in the flow to the actual characteristics of the wake as simulated. Section 2 includes a description of the simulations and the locations of the simulated DBS measurements.

Section 3 presents the calculations of DBS error, including quantification of error in the stream-wise, cross-stream, and vertical velocity components. In Sect. 4, we interpret these results and assess their implications for future measurements of complex flows like wind turbine wakes by instruments relying on the DBS method.

2 Data and methods

Because the probe length of the lidars considered here for use with the DBS method are on the order of tens of meters long, it is critical to resolve atmospheric eddies at that scale or finer to understand the effect of such eddies on the observations. It is also necessary to capture the time variability of these eddies. Therefore, it is necessary to employ LES, which explicitly resolves the largest scales of three-dimensional atmospheric turbulence and allows them to evolve in time. These eddies are responsible for most of the turbulent transport and turbulence kinetic energy production in the atmospheric boundary layer.

It is also necessary to represent the turbine and its effects on the flow. Our simulations are based on an incompressible LES solver that includes the effects of atmospheric stratification through the Boussinesq buoyancy approximation. The solver also incorporates an actuator line model to represent the effect of a wind turbine on the flow, similar to the simulations presented in Churchfield et al. (2012a). Actuator line models (Sørensen and Shen, 2002) represent turbine blades as separate rotating lines. Simulations from this LES-actuator line tool have been compared favorably to observations at the Lillgrund offshore wind farm (Churchfield et al., 2012b). Of course, any modeling study does incorporate some uncertainty in the model, but we have endeavored to minimize this uncertainty by using a validated LES with an actuator line model.

Although we have chosen to employ an actuator line model for this investigation, a similar approach could be taken with other LES capabilities that represent wind turbines as actuator disks, where the turbine rotor is represented by a permeable circular disk with uniformly distributed thrust forces (Calaf et al., 2010; Mirocha et al., 2014; Aitken et al., 2014b). Wu and Porté-Agel (2011) compare rotating and nonrotating actuator disk models with wind tunnel measurements and find satisfactory agreement between observations and rotating actuator disk models. Martínez-Tossas et al. (2015) compare actuator line and actuator disk models, concluding that they produce similar wake profiles although the actuator line model can generate flow structures near the blades such as root and tip vortices that the actuator disk model cannot. Using a curvilinear immersed boundary approach, Kang et al. (2014) conclude that the actuator line model is necessary for maintaining rotation within the wake and for accurately capturing the size and turbulence levels in the far wake, as well as for capturing wake meandering. Because of the potential role of wake meandering in defining the flow inhomogeneities that may affect lidar observations, we have chosen to use an actuator line model for this investigation.

2.1 Simulations of the stably stratified atmospheric boundary layer

The LES is performed using the Simulator fOr Wind Farm Applications (SOWFA; Churchfield and Lee, 2014) developed at the National Renewable Energy Laboratory. The simulations discussed here employ the same two-stage methodology as in Churchfield et al. (2012a), briefly summarized here. Turbulent atmospheric flow is generated using the LES solver on a domain with idealized periodic lateral boundaries, without turbines, to generate a precursor simulation. A plane of turbulent data from the upwind lateral boundary is saved at every time-step once the turbulent boundary layer has reached a quasi-equilibrium state. For the simulation here, quasi-equilibrium was reached at 1.8×10^4 s. Next, a turbine is introduced into the flow that has been initialized from the quasi-equilibrium precursor flow field. Upstream boundary conditions for this inner domain are provided by the saved planes of inflow data. The downstream boundary allows the turbine wake to exit without re-entering this turbine-resolving domain. More details on this procedure are presented in Churchfield et al. (2012a). For the simulations developed here, the precursor domain was 5000 m in the mean flow direction, 2500 m wide, and 750 m tall with 10 m grid resolution and a model time step of 0.025 s. The domain including the turbine was 3000 m in mean flow direction, 2500 m wide and 750 m tall. Grid resolution in the turbine domain telescoped from 10 to 5 to 2.5 to 1.25 m near the turbine (as seen in Fig. 1).

The turbine introduced into the model is similar to the GE 1.5-MW SLE deployed at the National Wind Technology Center (Clifton et al., 2013b). This upwind horizontal axis turbine has a three-bladed, 77 m rotor diameter (D) with a hub height of 80 m. Pitch and yaw angles are fixed relative to their neutral frame of reference; a variable speed torque controller is activated.

For this investigation of DBS error, we chose stable stratification because of the potential error introduced by the veering of wind with height. Additionally, because of the lower atmospheric turbulence level, turbine wakes persist farther downwind, allowing the influence of turbine wakes on lidar measurements using the DBS approach to be explored in more detail. The simulations included an imposed surface roughness of 0.1 m with a geostrophic wind that yielded an average wind speed at hub height approximately equal to $6.5\,\mathrm{m\,s^{-1}}$. In addition, a uniform initial potential temperature profile ($\theta(z)$) was specified, with $\theta = 300$ K for $z < 150$ m and $\mathrm{d}\theta/\mathrm{d}z = 0.01\,\mathrm{K\,m^{-1}}$ for $z > 150$ m, creating a capping inversion. Random perturbations were imposed at the outset on the mean velocity field within the boundary layer to

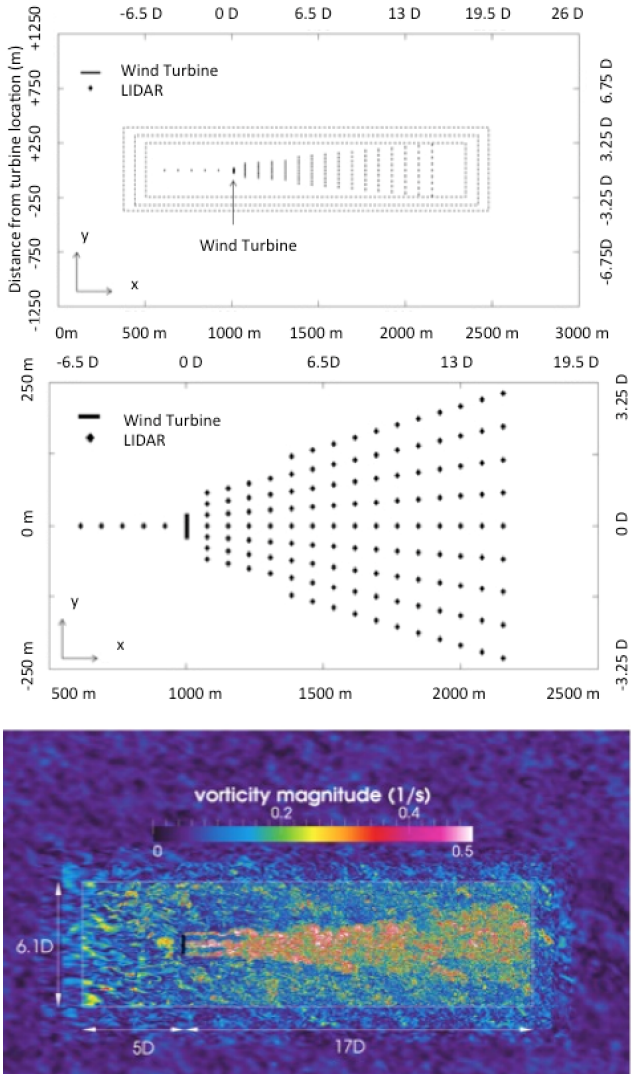

Figure 1. Simulation domain for precursor and turbine-resolving domains (top), with zoomed-in version (center) identifying lidar locations in the wake of the wind turbine and contours (bottom) of vorticity in the turbine-resolving domain. The nests (top) denote the regions with grid refinement from 10 to 5 to 2.5 to 1.25 m resolution. Flow is from west to east at the turbine hub height.

initiate the turbulent motion. With a surface cooling rate of $-1.4 \times 10^{-4}\,\mathrm{K\,s^{-1}}$ (or $0.5\,\mathrm{K\,h^{-1}}$), a slightly stable profile developed after the 1.8×10^4 s equilibration period, with a wind shear exponent α of 0.45 across the rotor disk and a change of wind direction of 15° across the rotor disk, accompanied by a turbulence intensity (TI) of 4.5 % at hub height (80 m). This case is based on the stable atmospheric boundary-layer observations collected with lidars during the Crop Wind Energy Experiment (CWEX) campaign (Rhodes and Lundquist, 2013).

The numerical simulations exhibit heterogeneities in the flow that will affect DBS observations. Contours of the velocity components along the wake centerline ($y = 0$ m or

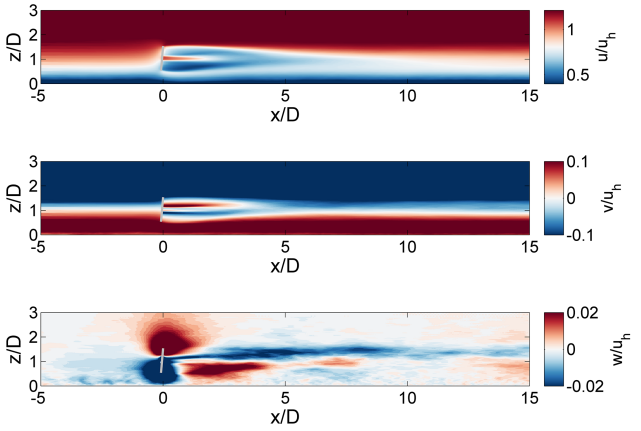

Figure 2. 10 min averaged contours of wind speed in the stream-wise (top), cross-stream (middle), and vertical (bottom) directions, normalized by average hub-height inflow wind speed ($6.5\,\mathrm{m\,s^{-1}}$), taken along the turbine location at $y = 0$ m (Fig. 1) after equilibration.

$y/D = 0$ in Fig. 1) show clear evidence of the turbine wake (Fig. 2). In the stream-wise component of the flow (top of Fig. 2), a wind speed deficit of 40 % is evident in both the top and bottom of the rotor disk. The wake wind speed is asymmetric, with a larger deficit in the bottom portion of the rotor disk as measured along this centerline. The deficit in the top portion of the rotor disk erodes quickly, likely because of the entrainment of faster-moving air aloft. The cross-stream component of the flow (middle of Fig. 2), upwind of the turbine, shows evidence of the veer in the simulation between the surface and levels above the turbine. Downwind of the turbine, counterclockwise rotation occurs within the first 4 D downwind of the turbine. In the vertical component of the flow (bottom of Fig. 2), rising motion is evident in the bottom part of the rotor disk with a narrow region of sinking motion just above hub height. The strongest impacts of the wake on vertical motion are not confined to only the first 5 D downwind. Instead, sinking motion in the top part of the wake extends past 10 D, likely contributing to the wake wind speed deficit recovery seen in the stream-wise component of the flow.

The nature of the wake circulations can more clearly be seen via cross-stream slices at selected downwind locations. (Note that these cross-stream slices are looking upwind.) The stream-wise component of the flow (Fig. 3) shows a distinct wake 3 D downwind of the turbine, with an asymmetric wind speed deficit as the wake itself has been stretched because of the mean shear of the flow. Recall that the wind direction changes 15° between the top and the bottom of the rotor disk. The wind speed within the wake is only 60 % of the inflow wind speed. By 5 D downwind, the wind speed has recovered in much of the top half of the rotor disk, but a deficit still exists in the bottom half of the rotor disk. Furthermore, the lateral boundaries of the wake have been stretched by the

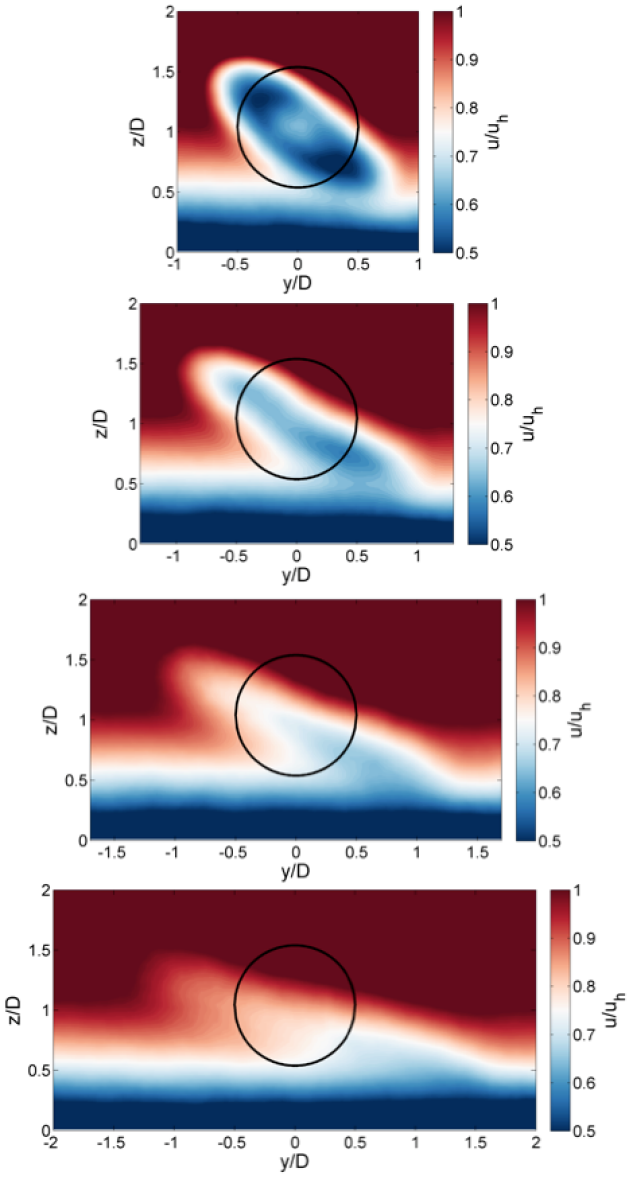

Figure 3. Cross-stream slices of stream-wise velocity, normalized by upwind hub-height wind speed ($6.5\,\mathrm{m\,s^{-1}}$) at $3\,D$ (top), $5\,D$, $7\,D$, and $10\,D$ (bottom) downwind of the turbine. The perspective is looking upwind. The large black circle outlines the location of the turbine rotor disk inscribed by the actuator line model.

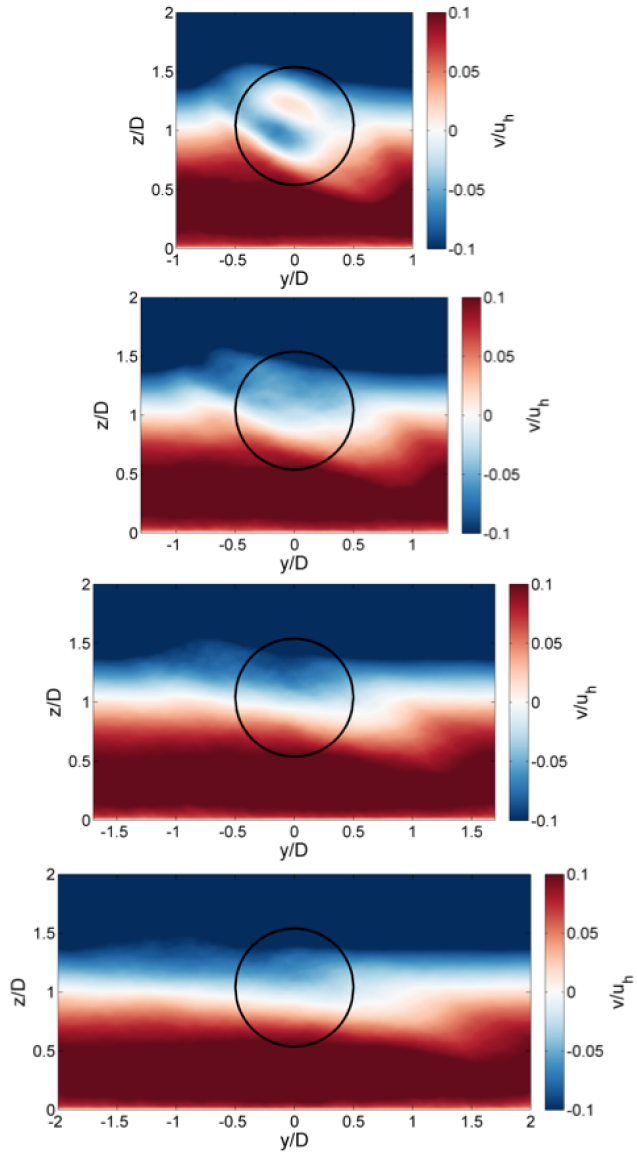

Figure 4. Cross-stream slices of cross-stream velocity, normalized by upwind hub-height wind speed ($6.5\,\mathrm{m\,s^{-1}}$) at $3\,D$ (top), $5\,D$, $7\,D$, and $10\,D$ (bottom) downwind of the turbine. The perspective is looking upwind. The large black circle outlines the location of the turbine rotor disk inscribed by the actuator line model.

mean flow. By $7\,D$ downwind, the wind speed in the bottom half of the rotor disk has recovered to 75 % of the upwind wind speed, while the largest wind speed deficit in the lower part of the rotor disk has been advected out of the boundary of the rotor disk. By $10\,D$ downwind, the evidence of the wake in the stream-wise component has been stretched and eroded by entrainment from the ambient flow. Although a wind speed deficit still exists in the lower levels, the original bimodal Gaussian-like shape of the wake is reduced to a small asymmetric signature of the wake deficit.

The cross-stream component of the flow (Fig. 4) shows evidence of the change of wind direction with height throughout the domain, as well as the rotation in the wake region. The counterclockwise rotation of the wake advects positive (negative) cross-stream components into the upper (lower) portion of the wake at $1\,D$ and $2\,D$ downstream (not shown), but by $3\,D$ downwind (top of Fig. 4), this mixing has been rapidly eroded. By $7\,D$ downwind, little evidence of the wake persists in the cross-stream component of the flow. The background shear has reestablished.

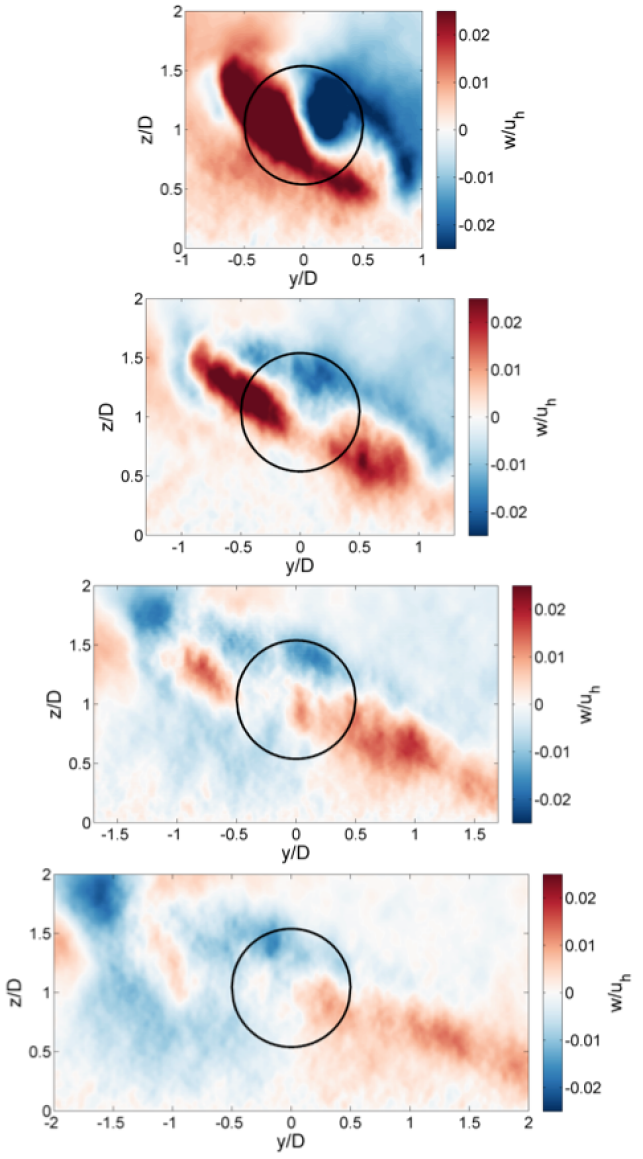

Figure 5. Cross-stream slices of vertical velocity, normalized by upwind hub-height wind speed (6.5 m s^{-1}) at 3 D (top), 5, 7, and 10 D (bottom) downwind of the turbine. The perspective is looking upwind. The large black circle outlines the location of the turbine rotor disk inscribed by the actuator line model.

The vertical component of the flow (Fig. 5) clearly exhibits the counterclockwise motion of the wake (recall that these slices are looking upwind). At 3 D downwind, sinking motion is evident on the $y/D > 0$ side of the wake, with rising motion on the $y/D < 0$ side. This circulation is stretched but still persists through 5 D downwind, but by 7 D downstream, the magnitudes of vertical velocities in the wake are greatly reduced. Little evidence of the wake, in terms of vertical velocities, remains by 10 D downwind.

The asymmetries in the flow will affect the retrievals of wind speed estimates using the DBS method.

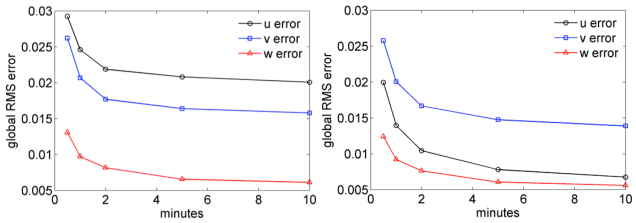

Figure 6. RMS global error (normalized by hub-height wind speed U_H of 6.5 m s^{-1}) at all lidar locations and all heights, normalized by the upwind hub-height wind speed, as a function of averaging time with the lidar range weighting function applied (left) and without the lidar range weighting function applied (right).

2.2 Lidar simulator method

To imitate the sampling approach of a lidar, probes were inserted into the flow field to measure LOS velocity components. In the DBS sampling technique, four beams, each at some angle θ from vertical (approximately 30°), are directed toward the north, east, south, and west, measuring the LOS velocity V_r of the flow along each beam denoted by subscripts V_{rN}, V_{rE}, V_{rS}, V_{rW}. The LES-calculated velocity vector (at 1.25 or 2.5 m resolution), described by components u, v, and w (stream-wise or west to east in Fig. 1, cross-stream or south to north, and vertical, respectively) is available at each grid cell in the domain. To calculate the LOS velocities V_{rN}, V_{rE}, V_{rS}, V_{rW}, we take the dot product of the LES-calculated velocity vector and the beam direction vector. Assuming horizontal homogeneity in the altitudes sampled, the system of wind equations becomes

$$u_L = \frac{V_{rE} - V_{rW}}{2\sin\theta}, \tag{1}$$

$$v_L = \frac{V_{rN} - V_{rS}}{2\sin\theta}, \tag{2}$$

and

$$w_L = \frac{V_{rN} + V_{rS} + V_{rE} + V_{rW}}{4\cos\theta}, \tag{3}$$

where u_L, v_L, and w_L describe the estimates of flow in the stream-wise (west to east in Fig. 1), cross-stream (south to north), and vertical directions where w is positive for upward motion.

To simulate measurement platforms within the computational domain, the LES velocity field (u, v, and w) was sampled at 1 Hz frequency at multiple locations upwind of the turbine, downwind of the turbine, and across the wake. At each instrument location, the samples were collected along the four slanted beams (slanted at $\theta = 30°$ from vertical) of a simulated vertical profiling lidar with 2.5 m vertical resolution. Two beams were aligned with the wind (V_{rE} V_{rW}), and along the wake, and the other two beams (V_{rN} V_{rS}), were perpendicular to the flow and across the wake. Additionally,

at each location, u, v, and w were sampled along a vertical "truth beam" of the same 2.5 m resolution. The beams all sampled to a maximum height of 200 m to match typical field capabilities of commercial lidars (Courtney et al., 2008; Aitken et al., 2012).

To reflect the actual operating conditions of the lidar, we apply the along-beam weighting function of the lidar to velocities V_{rN}, V_{rE}, V_{rS}, V_{rW} at a range of heights. As summarized by Cariou and Boquet (2010), Banakh and Smalikho (1997) derive the pulsed lidar range weighting function (RWF) along the beam distance z for a pulsed lidar to be

$$\mathrm{RWF}(z) = \frac{1}{c\tau_m}\left[\mathrm{erf}\left(\frac{4\sqrt{\ln(2)}}{c\tau}(z-z_0)+\frac{\sqrt{\ln(2)}\tau_m}{\tau}\right)\right.$$
$$\left.-\mathrm{erf}\left(\frac{4\sqrt{\ln(2)}}{c\tau}(z-z_0)-\frac{\sqrt{\ln(2)}\tau_m}{\tau}\right)\right], \quad (4)$$

where c is the speed of light, τ_m is the range gate (265 ns), τ is the full width half maximum (FWHM) (165 ns) pulse duration, and z_0 is the distance along the beam where the measurement is intended to be taken. This RWF is similar to that presented in Simley et al. (2014), and estimates range resolution of approximately 40 m, similar to estimates from Lindelöw (2007), who convolves the pulse and the range gate profile. The RWF is applied to the velocity estimates along the beam so that the estimate of a velocity at a particular altitude is actually a weighted sum of the velocities along a 40 m extent along that beam.

To these weighted estimates of velocities V_{rN}, V_{rE}, V_{rS}, V_{rW}, we apply the assumption of horizontal homogeneity reflected in Eqs. (1)–(2) to calculate the DBS estimates of u_{L}, v_{L}, and w_{L}. The estimated velocities u_{L}, v_{L}, and w_{L} can then be compared to the actual profiles of u, v, and w directly sampled from the LES field at the locations where the simulated lidar is measuring.

3 Quantification of DBS error in turbine wakes

Instruments were located upwind of the turbine to sample the inflow as well as across and on the edges of the wake, as seen in Fig. 1. We define error as the difference between the simulated measurements u_{L}, v_{L}, and w_{L} and the directly sampled truth measurements u, v, and w, which are based on the actual velocity profiles (not including weighting) above the instrument locations. In such cases, the error of a component is simply given by the difference between the components:

$$E_u = u - u_{\mathrm{L}}. \quad (5)$$

In other cases, it is useful to normalize these differences by the hub-height mean wind speed U_{H} of 6.5 m s^{-1}. As an error metric, we apply the root-mean-square (RMS) error of each velocity component, normalized by the hub-height wind speed U_{H}:

$$\mathrm{RMS}_u = \frac{\sqrt{(u-u_{\mathrm{L}})^2}}{U_{\mathrm{H}}}. \quad (6)$$

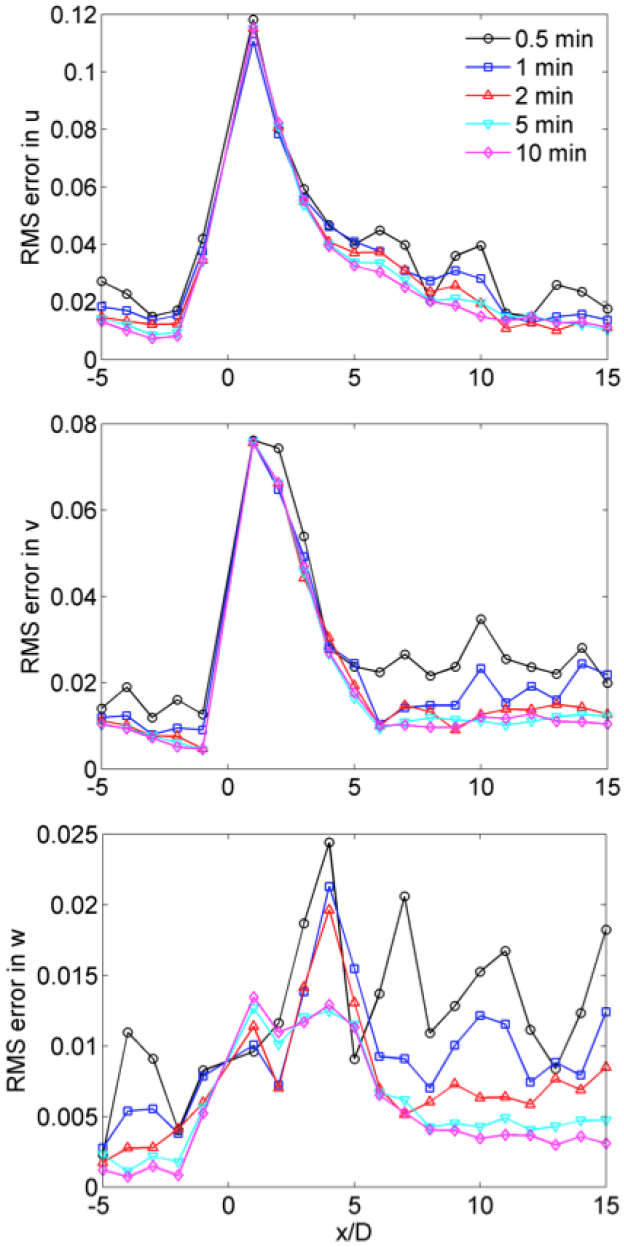

Figure 7. RMS global error (normalized by hub-height inflow wind speed U_{H} of 6.5 m s^{-1}) for each lidar situated along the turbine-wake centerline ($y = 0$ m and $y/D = 0$ in Fig. 1) with the lidar range weighting function applied. Stream-wise error (top), cross-stream error (middle), and vertical velocity error (bottom). Each color represents a different amount of time averaging.

Normalizing by each error component locally by the corresponding wind velocity component becomes problematic for the v and w components because those components can become very small. A global RMS is a simple summation.

We also wish to explore the effect of averaging time on error, or the convergence analysis of the statistics, as some error may be ameliorated by extending the sampling period.

Wakes are unsteady and meander laterally and vertically. Because of this unsteadiness and the resulting gradients, a single measurement in time is more vulnerable to error than the average of many measurements, and we attempt to quantify how error changes as averaging time is increased.

3.1 Global error and the effect of averaging time

First, we explore the effect of time averaging on error, recognizing that wakes are nonstationary processes that meander. To explore this effect of time averaging in a global sense, we can take the hub-height free-stream mean speed normalized RMS of the error (Eq. 6) at all the simulated instruments and at all heights. This approach provides a gross single value of error for the entire set of measurements (Fig. 6), both with and without the weighting function. For each velocity component, this error decreases when longer averaging times are employed; the error appears to approach an asymptote for averaging times between 5 and 10 min. When the lidar weighting function is applied (Fig. 6a), the error in the stream-wise (u-component) of the flow is largest, with a global error of approximately 3 % (normalized by hub-height inflow velocity) for averaging times less than 1 min. This large error is due to the large shear in the stream-wise component of the flow. Only slightly smaller is the error in the cross-stream (v-component) of the flow, approximately 2.5 %. All errors decrease with longer averaging time. (Errors for averaging times between 10 and 30 min were also tested, but errors only decreased negligibly compared to the 10 min average shown in Fig. 6.) Interestingly, when the lidar range weighting function is not applied (Fig. 6b), the cross-stream (v-component) error is the largest, followed by the stream-wise (u-component), and then the vertical (w-component). Because this error is averaged over all locations explored in these simulations, it is likely not an appropriate general metric. Instead, location-specific error metrics may be more appropriate for understanding specific measurement errors.

3.1.1 Error as a function of distance downstream

Perhaps the simplest case of error is that of the error along the wake centerline ($y = 0$ m in Fig. 1, or $y/D = 0$ in Fig. 3 through Fig. 5), and we can explore that error both as a function of distance downstream (expressed in terms of x/D where D is the turbine rotor diameter of 77 m) and as a function of averaging time (Fig. 7). Notably, upstream errors are nonzero, likely because of nonstationarity in the flow, but those errors become negligible for averaging times longer than 1 min in all components of the flow. Downwind of the turbine, the largest errors for all components occur in the near-wake region, between 0 D and 2 D downwind of the turbine, with the largest errors in the stream-wise component of the flow (Fig. 7, top). In fact, in this near-wake region, increasing the averaging time fails to decrease the error for all three components of the flow. However, upwind of the turbine and in the far-wake region, increasing the averaging time results in a reduction of error.

In the near-wake region, the DBS method is unable to accurately measure the flow regardless of averaging time because of the very large and persistent velocity gradients in this region, exacerbated by the lidar range weighting function. The v- and w-component error is large from 0 D to 5 D, even compared to the free-stream hub-height wind speed (as in Fig. 6). Wake rotation, characterized by the v- and w-velocity components, nearly vanishes beyond 5 D downstream (Figs. 4 and 5), so the reduction of error at distances past 5 D cannot be considered consequential. Therefore, measurements of wake rotation using the DBS method are questionable.

3.1.2 Error as a function of distance across the wake

Previous work (Bingöl et al., 2008, discussed further in Rhodes and Lundquist, 2013) has shown that, in homogeneous flow, DBS error in measurements of the stream-wise and cross-stream components of the flow is a function of vertical velocity. However, in a wind turbine wake, vertical velocities vary in magnitude and sign across the wake, with updrafts located on the left side looking upwind ($y/D < 0$) and downdrafts located on the right side looking upwind ($y/D > 0$). This inhomogeneity is further complicated in the stable case presented here as the wind direction changes with height such that the upper part of the wake is turned toward $y/D < 0$. As a result, larger errors in estimates of the stream-wise velocities occur on the $y/D < 0$ side of the wake (Fig. 8) even though longer averaging times clearly reduce error at most locations across the wake and at all distances downwind. The assessment of error also provides some evidence of the wake expansion as it moves downwind – the largest errors are expected to occur at the wake edges. The location of maximum error increase from $y = -0.6D$ (at $x/D = 3$) to $y = -0.8D$ (at $x/D = 5$) to $y = -1.0D$ (at $x/D = 9$) for the shortest averaging time. Of note, the location of maximum error is not the same for all averaging times, especially in the far-wake regions of $x/D \geq 7$, which we attribute to wake meandering at these distances.

At all distances downwind and all locations across the wake, the maximum normalized RMS error in the stream-wise component is less than 8 % of the free-stream hub-height wind speed, considering all heights within the rotor disk. Wake velocity deficits are on the order of 40 % of the free-stream hub-height wind speed.

While the stream-wise component manifests largest errors at the edges of the wake, the cross-stream component shows largest errors within the wake, due to the significant cross-stream gradients induced by rotation in the wake (Fig. 9). Especially at $x/D = 3$, the maximum error (approximately 5 %, normalized by the hub-height inflow wind speed) is found within the wake itself. As the wake propagates downwind and the wake-induced gradients decay, errors are reduced.

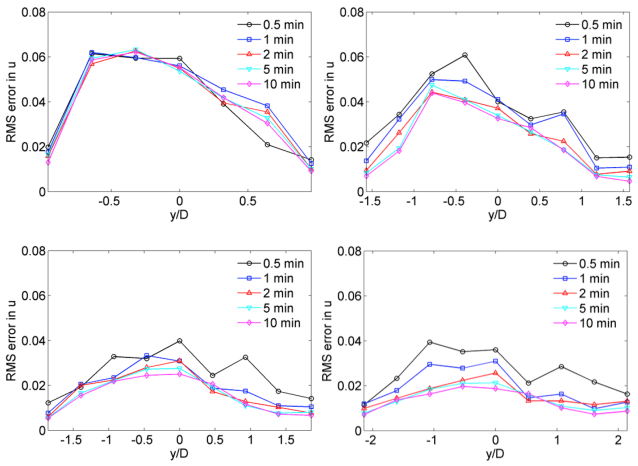

Figure 8. RMS global error (normalized by hub-height inflow wind speed U_H of $6.5\,m\,s^{-1}$) in the stream-wise component across the wake at different distances downstream: $x/D = 3$ (top left), $x/D = 5$ (top right), $x/D = 7$ (bottom left), $x/D = 9$ (bottom right) with the lidar range weighting function applied; the different colors denote averaging times.

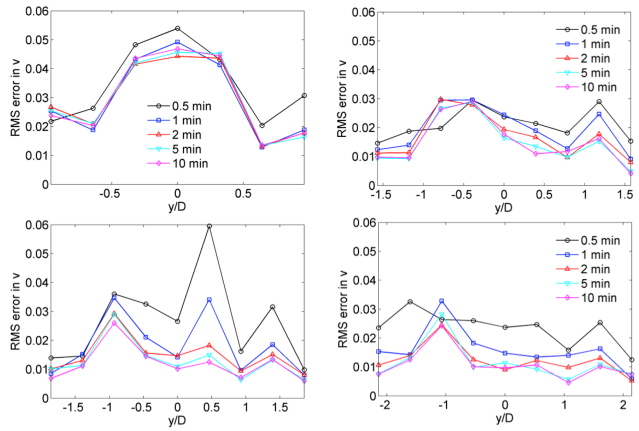

Figure 9. RMS global error (normalized by hub-height inflow wind speed U_H of $6.5\,m\,s^{-1}$) in the cross-stream component across the wake at different distances downstream with the lidar range weighting function applied: $x/D = 3$ (top left), $x/D = 5$ (top right), $x/D = 7$ (bottom left), $x/D = 9$ (bottom right); the different colors denote averaging times.

The largest errors tend to be found on the $y/D < 0$ side of the wake (as in the stream-wise component) for all averaging times greater than 1 min.

3.2 Velocity error as a function of height along the wake centerline

Comparisons of the DBS-retrieved velocities to the actual velocities along the wake centerline emphasize the limitations of the DBS method even in the center of the wake (Fig. 10). The stream-wise velocity estimates (left panels) are based on the two beams parallel to the stream-wise flow. In the strong vertical gradients of the near-wake region, the errors are significant, mostly due to the lidar range weighting function. For the cross-stream component (middle panels of Fig. 10), the rotation of the wake is eliminated by the DBS method at both 3 D and 5 D downwind of the turbine, although the general change of wind direction with height in the domain is reasonably well-captured by the DBS method. The inhomogeneities in the wake are not captured by the DBS method, but these inhomogeneities reduce as the wake propagates downstream. Therefore, by 7 D downstream (not shown), when the cross-stream components again become small, the errors between the DBS estimates and the actual cross-stream velocity become negligible. Similarly, the errors in DBS estimates of the vertical velocity between the turbine and 5 D downwind are of the same order as the vertical velocity itself (right panels of Fig. 10) because of the large vertical velocities in the near-wake region. Even by 7 D downstream, agreement between the DBS estimates of vertical velocity and the actual vertical velocity has not been attained along the wake centerline.

3.3 Velocity error profiles across the wake

Large inhomogeneities are expected at the edge of the wake because of the contrast between the wake flow and the free stream flow. We also expect inhomogeneities in the center of the wake caused by the wake rotation. To quantify the error in wind speed estimates based on the DBS approach, we inspect the profiles of error (Eq. 5) at instruments located on the edges of the wake in comparison to the errors from locations in the center of the wake (along $y/D = 0$).

The largest errors are found in the row of instruments closest to the turbine, at $x/D = 1$ (Fig. 11, top row). The stream-wise errors (top left panel of Fig. 11) on the edges of the wake are on the order of $1\,m\,s^{-1}$ or 15 % of the hub-height inflow velocity. At the center of the wake, the stream-wise errors are even larger, on the order of $2\,m\,s^{-1}$ or 30 % of the hub-height inflow velocity. The cross-stream velocity errors (top center panel of Fig. 11) are considerable throughout the wake, approaching $1\,m\,s^{-1}$ (15 % when normalized with inflow hub-height velocity) in the center of the wake, with smaller errors due to the lidar range weighting function at the edges of the wake. (Without the lidar range weighting function, the largest errors in cross-stream velocity estimates occurred at the wake edges.) The vertical velocities (top right panel of Fig. 11) are generally overestimated on the side of the wake with rising motion (black line, $y/D < 0$) and underestimated on the side of the wake with sinking motion (red line, $y/D > 0$).

These errors decrease as the wake propagates downwind of the turbine. By 3D downwind (center row of Fig. 11), the maximum error in the stream-wise component (center left panel) is less than $1.0\,m\,s^{-1}$ (15 % when normalized with inflow hub-height velocity), with the greatest error near the top of the rotor disk for a measurement at the edge of the wake on

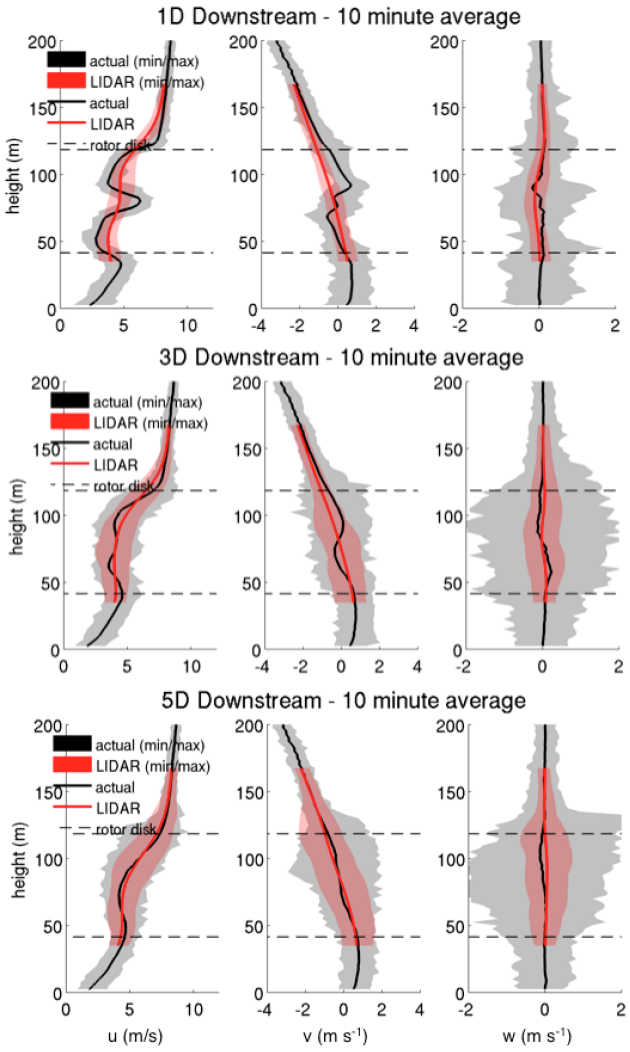

Figure 10. Vertical profiles of the stream-wise (left), cross-stream (middle), and vertical (right) components of wind speed at different locations downstream of the turbine on the wake centerline $y/D = 0$ as measured by the simulated lidars with weighting function applied (red lines) and directly sampled from the LES (black line). The shaded regions represent the envelope of all sampled values from the simulated lidar (pink) and from the direct LES sampling (gray).

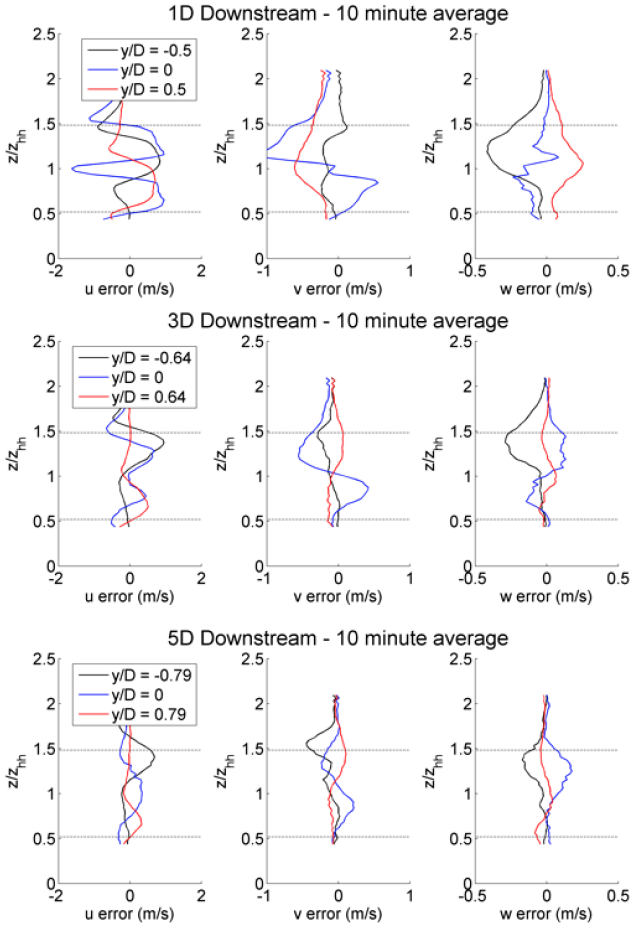

Figure 11. Profiles of error (Eq. 5) in lidar measurements of stream-wise (left), cross-stream (center), and vertical (right) wind speed, with the lidar range weighting function applied, from lidars located 1 D (top), 3 D (center), and 5 D (bottom) downwind of the turbine. Locations of the lidars are at the center and the cross-stream edges of the wakes as labeled in the figures.

the rising side. The cross-stream component (center panel) error is also reduced, near $0.5\,\mathrm{m\,s^{-1}}$ (8 % when normalized) in the center of the wake and on the order of $0.25\,\mathrm{m\,s^{-1}}$ (4 %) at the wake edges. The DBS estimates of the vertical velocity component (center right panel) exaggerate the rising motion near the top of the rotor disk on the side of the wake with rising motion (black line, $y/D < 0$). The DBS error also overestimates vertical motion in the bottom of the rotor disk on the side of the turbine with general sinking motion. Because the errors in estimates of vertical motion are on the order of the vertical velocities themselves, the DBS approach should not be considered reliable for estimates of vertical velocities in this region of the wake.

Farther downwind, errors are generally reduced. At $5D$ downwind (bottom row of Fig. 11), the largest percentage error is in the vertical component (bottom left panel) from the lidar located near the centerline, although the cross-stream errors are still large in the center of the wake and at the top of the rotor disk at the location on the rising side of the wake.

4 Discussion and conclusions

Numerous commercial lidar and sodar systems use a DBS technique to estimate winds for wind energy, air quality, and urban meteorology applications. Using LES of stable atmospheric boundary-layer flow past a wind turbine, we have quantified the error expected from observations collected using the DBS measurement approach in the vicinity of a wind turbine wake. The three-component velocity vectors calcu-

lated by the LES are converted into LOS velocities representative of lidar technology using four beams, an appropriate lidar range weighting function, and the DBS method. These LOS velocities are then used to calculate the wind field estimates that would have been observed by instruments located within this flow. The difference between these DBS estimates of winds and the actual wind profiles at the instrument locations are used to quantify the error that can be expected from the application of the DBS approach in heterogeneous flow. This quantification of error in DBS measurements is subject to uncertainty of the large-eddy simulation model; the model selected here has been validated with respect to standard boundary-layer studies and power measurements within a large wind farm (Chuchfield et al. 2012b).

These stable atmospheric boundary-layer simulations represent a very challenging scenario of single-instrument measurement error, given the heterogeneous flow across the measurement volume resulting from the wind turbine wake, as well as the significant (15°) change of wind direction across the altitudes of the turbine rotor disk with rotor diameter D. These results provide reasonable error bounds for remote sensing observations of wind turbine wakes using the DBS approach. For the case simulated here, time averaging of the observations of at least 5 min can eliminate some of the error in the observations, notably for the upwind measurements and the far downwind measurements ($x > 5D$) aligned with the flow along the wake centerline.

The largest DBS-related errors are found in the near-wake region, between the turbine and 2 D downwind of the turbine, and at locations where the wake rotation induces significant cross-stream and vertical velocities (both the wake edges and along the wake centerline). Stream-wise velocity errors in this near-wake region are on the order of 30 % of the hub-height inflow wind speed (2.0 m s^{-1}) at 1 D and 2 D downwind in the regions of the rotor disk altitudes. Cross-stream velocity errors are on the order of 15 % of the hub-height inflow wind speed (1.0 m s^{-1}) and the vertical velocity errors are on the order of 0.2 m s^{-1} (in excess of actual vertical velocities). Therefore, DBS-based assessments of wake wind speed deficits based on the stream-wise velocity in conditions such as those simulated here can be relied on even within the near wake only within 2.0 m s^{-1}, or 30 % of the hub-height inflow wind speed, and cross-stream and vertical velocity estimates in the near wake are also compromised, on the order of 15 % or greater. These errors are larger for shorter time-averaging periods for these equilibrated and stationary simulations. Of course, part of the near-wake error is due to the fact that the DBS beams may be sampling outside of the wake, especially in the upper portion of the rotor disk. This error can be accounted for in the analysis of results (Rhodes and Lundquist, 2013). Outside of the near-wake region, by $\sim 3\,D$ downwind, errors in the stream-wise component are reduced to ~ 15 % of the hub-height inflow wind speed.

The results presented here include the effect of the lidar range weighting function (RWF), a convolution of the pulse power profile and the range gate profile. Our first set of calculation ignored this RWF, and it is interesting to note that the errors were much smaller without the RWF. The inhomogeneous flow of the wind turbine wake contains large vertical gradients of wind speed and wind direction, which are effectively smoothed by the RWF. In the case of the stream-wise component of the flow, this smoothing exaggerates DBS errors while this smoothing reduces DBS errors for the cross-stream and vertical components of the flow.

The DBS approach has been used to characterize wind turbine wakes with sodar (Barthelmie et al., 2003) and with lidar (Nygaard, 2011; Rhodes and Lundquist, 2013; Kumer et al., 2013), and has also been applied to complex urban flows (Lane et al., 2013). As shown here, measurements of inhomogeneous flow such as wind turbine wakes are vulnerable to errors, and interpretations of field observations should account for this uncertainty, beyond the uncertainty in the radial velocity measurements provided by the manufacturers of the instruments. The limitations presented here do not undermine the benefits of DBS-based systems, which include the ability to rapidly profile winds at multiple altitudes simultaneously. In fact, we suggest that combining DBS-style instruments with more flexible instruments such as scanning lidar that can use scans with other geometries to measure winds can enable greater insight into complex flows like wind turbine wakes (as in Smalikho et al., 2013; Aitken et al., 2014a). Comparisons between in situ instruments such as unmanned aerial systems (Lawrence and Balsley, 2013) and DBS-based instruments can also help bound uncertainty.

The methodology presented here, which uses LES to calculate simulated observations, can be refined and extended to other applications. A lidar simulator such as employed here could also be used to test the utility of the fifth vertical beam now employed by some lidar manufacturers to supplement the DBS method (Wagner and Bejdić, 2014). The effects of the turbine tower, nacelle, and rotor tilt could be included (as in the actuator disk modeling of Aitken et al., 2014b). Simulation capabilities that fully resolve all elements of the turbine (Kang et al., 2014) can be compared with our results to determine if there are important effects from tip vortices. Because lidars are being used in urban meteorology (Lane et al., 2013), it is important to establish how the complex and heterogeneous flow in urban areas affects the error in the DBS technique used there. LES capabilities can also be used to interpret observations from other platforms, such as scanning lidar or unmanned aerial systems. Finally, new approaches to atmospheric modeling in complex terrain (Lundquist et al., 2012) could also be used to quantify observational uncertainty of DBS-based instruments for flow in complex terrain.

Acknowledgements. This work was supported by the US Department of Energy (DOE) under Contract No. DE-AC36-08GO28308 with the National Renewable Energy Laboratory. The DOE Office of Energy Efficiency and Renewable Energy, Wind and Water Power Technologies Office provided funding for the work. The authors express appreciation to Branko Kosović, three anonymous reviewers, and Valerie Kumer for helpful comments on the manuscript. The simulations were performed using computational resources sponsored by DOE's Office of Energy Efficiency and Renewable Energy and located at the National Renewable Energy Laboratory.

Edited by: L. Bianco

References

Aitken, M. L., Rhodes, M. E., and Lundquist, J. K.: Performance of a wind-profiling lidar in the region of wind turbine rotor disks, J. Atmos. Ocean. Tech., 29, 347–355, 2012.

Aitken, M. L., Banta, R. M., Pichugina, Y. L., and Lundquist, J. K.: Quantifying wind turbine wake characteristics from scanning remote sensor data, J. Atmos. Ocean. Tech., 31, 765–787, doi:10.1175/JTECH-D-13-00104.1, 2014a.

Aitken, M. L., Kosovic, B., Mirocha, J., and Lundquist, J. K.: Large-eddy simulation of wind turbine wake dynamics in the stable boundary layer using the Weather Research and Forecasting Model, J. Renew. Sustain. Ener., 6, 033137, doi:10.1063/1.4885111, 2014b.

Banakh, V. A. and Smalikho, I. N.: Estimation of turbulent energy dissipation rate from data of pulse Doppler lidar, Atmos. Oceanic Opt., 10, 957–965, 1997.

Barthelmie, R. J., Folkerts, L., Ormel, F. T., Sanderhoff, P., Eecen, P. J., Stobbe, O., and Nielsen, N. M.: Offshore wind turbine wakes measured by sodar, J. Atmos. Ocean. Tech., 20, 466–477, doi:10.1175/1520-0426(2003)20<466:OWTWMB>2.0.CO;2, 2003.

Bezault, C. and Boquet, M.: Sensitivity of the CFD-based LIDAR correction, European Wind Energy Association (EWEA) poster 167, 14–17 March 2011, Brussels, Belgium, available at: http://proceedings.ewea.org/annual2011/posters/PO.167_EWEA2011presentation.pdf, (last access: 14 February 2015), 2011.

Bingöl, F., Mann, J., and Foussekis, D.: Modeling conically scanning lidar error in complex terrain with WAsP Engineering, Danmarks Tekniske Universitet, Risø Nationallaboratoriet for Bæredygtig Energi, 16 p. (Denmark. Forskningscenter Risoe. Risoe-R; No. 1664(EN)), available at: http://orbit.dtu.dk/services/downloadRegister/3332817/ris-r-1664.pdf, (last access: 14 February 2015), 2008.

Bingöl, F., Mann, J., and Foussekis, D.: Conically scanning lidar error in complex terrain, Meteorol. Z., 18, 189–195, doi:10.1127/0941-2948/2009/0368, 2009.

Boquet, M., Ribstein, B. R., Parmentier, R. P., Sauvage, L. S., and Cariou, J.-P. C.: Theoretical and CFD analysis of pulsed Doppler lidar wind profile measurement process in complex terrain, Proceedings of the EWEA European Wind Energy Conference, 20–23 April 2010, Warsaw, Poland.

Bradley, S., Perrott, Y., Behrens, P. and Oldroyd, A.: Corrections for wind-speed errors from sodar and lidar in complex terrain, Bound.-Lay. Meteorol., 143, 37–48, 2012.

Butler, J. and Quail, F.: Comparison of a 2nd generation LiDAR wind measurement technique with CFD numerical modelling in complex terrain, International Conference on Sustainable Power Generation and Supply (SUPERGEN 2012), 1–6, 8–9 September 2012, Hangzhou, China, available at: http://ieeexplore.ieee.org/stamp/stamp.jsp?tp=&arnumber=6493088&isnumber=6493060, doi:10.1049/cp.2012.1769, (last access: 14 February 2015), 2012.

Calaf, M., Meneveau, C., and Meyers, J.: Large-eddy simulation study of fully developed wind-turbine array boundary layers, Phys. Fluids, 22, 015110, doi:10.1063/1.3291077, 2010.

Cariou, J.-P. and Boquet, M: LEOSPHERE Pulsed Lidar Principles: Contribution to UpWind WP6 on Remote Sensing Devices, 1–32, available at: http://www.upwind.eu/Publications/~/media/UpWind/Documents/Publications/6%20-%20Remote%20Sensing/D611.ashx, (last access: 14 February 2015), 2010.

Cariou, J.-P.: Pulsed lidars, in Remote Sensing for Wind Energy. Risø report Risø-I-3184(EN), Risø National Laboratory for Sustainable Energy, edited by: Peña, A. and Hasager, C. B., Risø National Laboratory for Sustainable Energy, Technical University of Denmark, Roskilde, Denmark, May 2011, 65–81 pp.

Cheong, B. L., Yu, T.-Y., Paler, R. D., Yang, K.-F., Hoffman, M. W., Frasier, S. J., and Lopez-Dekker, F. J.: Effects of Wind Field Inhomogeneities on Doppler Beam Swinging Revealed by an Imaging Radar, J. Atmos. Ocean. Tech., 25, 1414–1422, 2008.

Churchfield, M. J., Lee, S., Michalakes, J., and Moriarty, P. J.: A numerical study of the effects of atmospheric and wake turbulence on wind turbine dynamics, J. Turbul., 13, 1–32, 2012a.

Churchfield, M. J., Lee, S., Moriarty, P. J., Martínez, L. A., Leonardi, S., Vijayakumar, G., and Brasseur, J. G.: A large-eddy simulation of wind-plant aerodynamics, AIAA Aerospace Sciences Meeting including the New Horizons Forum and Aerospace Exhibition, Nashville, Tennessee, 9–12 January 2012, AIAA Paper 2012–537, 2012b.

Churchfield, M. J. and Lee, S.: Simulator fOr Wind Farm Applications, available at: http://wind.nrel.gov/designcodes/simulators/sowfa/, (last access: 14 February 2015), 2014.

Clifton, A., Elliott, D., and Courtney, M. (Eds.): Ground- based vertically-profiling remote sensing for wind resource assessment. Number 15 in Expert Group Study on Recommended Practices, International Energy Agency, 1st Edn., available at: http://www.ieawind.org/index_page_postings/RP/RP%2015_RemoteSensing_1stEd_8March2013.pdf, (last access: 14 February 2015), 2013a.

Clifton, A., Schreck, S., Jager, D., Kelley, N., and Lundquist, J. K.: Meteorological tower observations at the National Renewable Energy Laboratory, J. Sol. Energ.-T. ASME, 135, 3, 031017, doi:10.1115/1.4024068, 2013b.

Courtney, M., Wagner, R., and Lindelöw, P.: Testing and comparison of lidars for profile and turbulence measurements in wind energy, IOP Conf. Ser., Earth Environ. Sci., 1, 012021, doi:10.1088/1755-1315/1/1/012021, 2008.

Fuertes, F. C., Iungo, G. V., and Porté-Agel, F.: 3D turbulence measurements using three synchronous wind lidars: validation against sonic anemometry, J. Atmos. Ocean. Tech., 31, 1549–1556, doi:10.1175/JTECH-D-13-00206.1, 2014.

Gkanias, A., Papatolios, K., Konstantinidis, D., Karagiannis, G., and Katsanevakis, A.: A comparison of wind flow over complex terrain using CFD simulation and lidar measurements, available at: http://proceedings.ewea.org/annual2011/allfiles2/1363_EWEA2011presentation.pdf, (last access: 14 February 2015), 2011.

Gottschall, J., Courtney, M. S., Wagner, R., Jørgensen, H. E., and Antoniou, I.: Lidar profilers in the context of wind energy – a verification procedure for traceable measurements, Wind Energy, 15, 147–159, doi:10.1002/we.518, 2012.

Harris, M., Locker, I., Douglas, N., Girualt, R., Abiven, C., and Brady, O.: Validated adjustment of remote sensing bias in complex terrain using CFD, European Wind Energy Conference, 20–23 April 2010, Warsaw, Poland.

Hasager, C. B., Stein, D., Courtney, M., Peña, A., Mikkelsen, T., Stickland, M., and Oldroyd, A.: Hub height ocean winds over the North Sea observed by the NORSEWInD lidar array: measuring techniques, quality control and data management, Remote Sens., 5, 4280–4303, 2013.

Iungo, G. V., Wu, Y.-T., and Porté-Agel, F.: Field measurements of wind turbine wakes with lidars, J. Atmos. Ocean. Tech., 30, 274–287, doi:10.1175/JTECH-D-12-00051.1, 2013.

Kang, S., Yang, X., and Sotiropoulos, F.: On the onset of wake meandering for an axial flow turbine in a turbulent open channel flow, J. Fluid Mech., 744, 376–403, doi:10.1017/jfm.2014.82, 2014.

Khadiri-Yazami, Z., Pauscher, L., Klaas, T., Prus, S., and Lange, B.: Realization of a virtual met mast using three pulsed lidars on maneuverable tilting platforms, EWEA Proceedings, Vienna, Austria, 4–7 February 2013, available at: http://proceedings.ewea.org/annual2013/proceedings/Posters/PO_257_EWEA2013presentation.pdf, 2013.

Käsler, Y., Rahm, S., Simmet, R., and Kühn, M.: Wake measurements of a multi-MW wind turbine with coherent long-range pulsed Doppler wind lidar, J. Atmos. Ocean. Tech., 27, 1529–1532, 2010.

Krishnamurthy, R., Choukulkar, A., Calhoun, R., Fine, J., Oliver, A., and Barr, K. S.: Coherent Doppler lidar for wind farm characterization, Wind Energy, 16, 189–206, doi:10.1002/we.539, 2013.

Kumer, V.-M., Grubisic, V., Dorninger, M., Serafin, S., Strauss, L., and Zauner, R.: Turbulence analysis of lidar wind measurements at a wind park in lower Austria. EWEA Proceedings, Vienna, Austria, 4–7 February, 2013, available at: http://proceedings.ewea.org/annual2013/proceedings/Posters/PO_256_EWEA2013presentation.pdf, 2013.

Lane, S. E., Barlow, J. F., and Wood, C. R.: An assessment of a three-beam Doppler lidar wind profiling method for use in urban areas, J. Wind Eng. Ind. Aerod., 119, 53–59, doi:10.1016/j.jweia.2013.05.010, 2013.

Lawrence, D. A. and Balsley, B. B.: High-resolution atmospheric sensing of multiple atmospheric variables using the DataHawk Small Airborne Measurement System, J. Atmos. Ocean. Tech., 30, 2352–2366, 2013.

Lindelöw, P.: Fiber based coherent lidars for remote wind sensing, PhD thesis, Technical University of Denmark (DTU), Lyngby, Denmark, available at: http://orbit.dtu.dk/fedora/objects/orbit:82438/datastreams/file_4957725/content, (last access: 14 February 2015), 2007.

Lundquist, K. A., Chow, F. K., and Lundquist, J. K.: An immersed boundary method enabling large-eddy simulations of urban terrain in the WRF model, Mon. Weather Rev., 140, 3936–3955, 2012.

Mann, J., Cariou, J.-P., Courtney, M., Parmentier, R., Mikkelsen, T., Wagner, R., Lindelöw, P., Sjöholm, M., and Enevoldsen, K.: Comparison of 3D turbulence measurements using three staring wind lidars and a sonic anemometer, IOP Conference Series: Earth and Environmental Science, 1, 012012, available at: http://stacks.iop.org/1755-1315/1/i=1/a=012012, 2008.

Martínez-Tossas, L. A., Churchfield, M. J., and Leonardi, S.: Large-eddy simulations of flow past wind turbines: actuator line and disk modelling, Wind Energy, doi:10.1002/we.1747, 2015.

Meissner, C. and Boquet, M.: Correction of lidar remote sensing measurements by CFD simulation, EWEA Poster 196, Brussels, Belgium, 14–17 March 2011, available at: http://www.windsim.com/documentation/EWEA_pres_2011/Correction%20of%20LIDAR%20remote%20sensing%20measurements%20by%20CFD%20simulations.pdf, 2011.

Mikkelsen, T., Mann, J., Courtney, M., and Sjöholm, M.: Windscanner: 3-D wind and turbulence measurements from three steerable Doppler lidars, IOP C. Ser. Earth Env., 1, 012018, doi:10.1088/1755-1307/1/1/012018, 2008.

Mirocha, J., Kosovic, B., Aitken, M., and Lundquist, J. K.: Implementation of a generalized actuator disk wind turbine model into WRF for large-eddy simulation applications, J. Renewable Sustainable Energy, 6, 013104, doi:10.1063/1.4861061, 2014.

Newsom, R. K., Ligon, D., Calhoun, R., Heap, R., Cregan, E., and Princevac, M.: Retrieval of microscale wind and temperature fields from single- and dual-Doppler lidar data, J. Appl. Meteorol., 44, 1324–1345, 2005.

Newsom, R. K., Berg, L. K., Shaw, W. J., and Fischer, M. L.: Turbine-scale wind field measurements using dual-Doppler lidar, Wind Energy, 18, 219–235, doi:10.1002/we.1691, 2015.

Nygaard, N. G.: Lidar wake measurements in an onshore wind farm. VindKraftNet: Remote Sensing Workshop, Roskilde, Denmark, available at: http://www.windpower.org/download/1295/06_DONG_Lidar_wake_measurements_in_an_onshore_wind_farm.pdf, (last access: 14 February 2015), 2011.

Rajewski, D. A., Takle, E. S., Lundquist, J. K., Oncley, S., Prueger, J. H., Horst, T. W., Rhodes, M. E., Pfeiffer, R., Hatfield, J. L., Spoth, K. K., and Doorenbos, R. K.: Crop Wind Energy Experiment (CWEX): observations of surface-layer, boundary layer, and mesoscale interactions with a wind farm, B. Am. Meteorol. Soc., 94, 655–672, doi:10.1175/BAMS-D-11-00240.1, 2013.

Rhodes, M. E. and Lundquist, J. K.: The effect of wind turbine wakes on summertime Midwest atmospheric wind profiles, Bound.-Lay. Meteorol., 149, 85–103, doi:10.1007/s10546-013-9834-x, 2013.

Sathe, A. and Mann, J.: A review of turbulence measurements using ground-based wind lidars, Atmos. Meas. Tech., 6, 3147–3167, doi:10.5194/amt-6-3147-2013, 2013.

Sathe, A., Mann, J., Gottschall, J., and Courtney, M.: Can wind lidars measure turbulence?, J. Atmos. Ocean. Tech., 28, 7, 853–868, doi:10.1175/JTECH-D-10-05004.1, 2011.

Simley, E., Pao, L. Y., Frehlich, R., Jonkman, B., and Kelley, N.: Analysis of light detection and ranging wind speed measurements for wind turbine control, Wind Energy, 17, 413–433, doi:10.1002/we.1584, 2014.

Smalikho, I. N., Banakh, V. A., Pichugina, Y. L., Brewer, W. A., Banta, R. M., Lundquist, J. K., and Kelley, N. D.: Lidar investigation of atmosphere effect on a wind turbine wake, J. Atmos. Ocean. Tech., 30, 2554–2570, doi:10.1175/JTECH-D-12-00108.1, 2013.

Sørensen, J. N. and Shen, W. Z.: Numerical modelling of wind turbine wakes, J. Fluid. Eng.-T. ASME, 124, 393–399, 2002.

Stawiarski, C., Träumner, K., Knigge, C., and Calhoun, R.: Scopes and challenges of dual-Doppler lidar wind measurements – an error analysis, J. Atmos. Ocean. Tech., 30, 2044–2062, doi:10.1175/JTECH-D-12-00244.1, 2013.

Wagner, R. and Bejdić, J.: Windcube + FCR test in Hrgud, Bosnia & Herzegovina Final report, DTU Wind Energy E-0039, available at: http://orbit.dtu.dk/fedora/objects/orbit:129671/datastreams/file_5989924c-e951-4844-9d1e-706b4122b32c/content, (last access: 14 February 2015), 2014.

Wainwright, C. E., Stepanian, P. M., Chilson, P. B., Palmer, R. D., Fedorovich, E., and Gibbs, J. A.: A time series sodar simulator based on large-eddy simulation, J. Atmos. Ocean. Tech., 31, 876–889, doi:10.1175/JTECH-D-13-00161.1, 2014.

Wu, Y.-T. and Porté-Agel, F.: Large-eddy simulation of wind-turbine wakes: evaluation of turbine parameterisations, Bound.-Lay. Meteorol., 138, 345–366, 2011.